



CHORUS

This is the accepted manuscript made available via CHORUS. The article has been published as:

Routing Single Photons from a Trapped Ion Using a Photonic Integrated Circuit

Uday Saha, James D. Siverns, John Hannegan, Mihika Prabhu, Qudsia Quraishi, Dirk Englund, and Edo Waks

Phys. Rev. Applied **19**, 034001 — Published 1 March 2023

DOI: [10.1103/PhysRevApplied.19.034001](https://doi.org/10.1103/PhysRevApplied.19.034001)

Routing Single Photons from a Trapped Ion Using a Photonic Integrated Circuit

Uday Saha^{1,2}, James D. Siverns^{1,2,3}, John Hannegan^{2,3}, Mihika Prabhu⁴, Qudsia Quraishi^{5,2,6}, Dirk Englund⁴, Edo Waks^{1,2,3,6*}

¹Department of Electrical and Computer Engineering, University of Maryland College Park, MD, 20742.

²Institute for Research in Electronics and Applied Physics (IREAP), University of Maryland, College Park, MD, 20742.

³Department of Physics, University of Maryland College Park, MD, 20742.

⁴Department of Electrical Engineering and Computer Science, Massachusetts Institute of Technology, Cambridge, MA, 02139.

⁵United States Army Research Laboratory, Adelphi, MD, 20783.

⁶Joint Quantum Institute (JQI), University of Maryland, College Park, MD, 20742.

*Corresponding Author: edowaks@umd.edu

Abstract

Trapped ions are promising candidates for nodes of a scalable quantum network due to their long-lived qubit coherence times and high-fidelity single and two-qubit gates. Future quantum networks based on trapped ions will require a scalable way to route photons between different nodes. Photonic integrated circuits from fabrication foundries provide a compact solution to this problem. However, these circuits typically operate at telecommunication wavelengths which are incompatible with the strong dipole emissions of trapped ions. In this work, we demonstrate the routing of single photons from a trapped ion using a photonic integrated circuit. We employ quantum frequency conversion to match the emission of the ion to the operating wavelength of a foundry-fabricated silicon nitride photonic integrated circuit, achieving a total transmission of $31.0 \pm 0.9\%$ through the device. Using programmable phase shifters, we switch the single photons between the output channels of the circuit and also demonstrate a 50/50 beam splitting condition. These results constitute an important step towards programmable routing and entanglement distribution in large-scale quantum networks and distributed quantum computers.

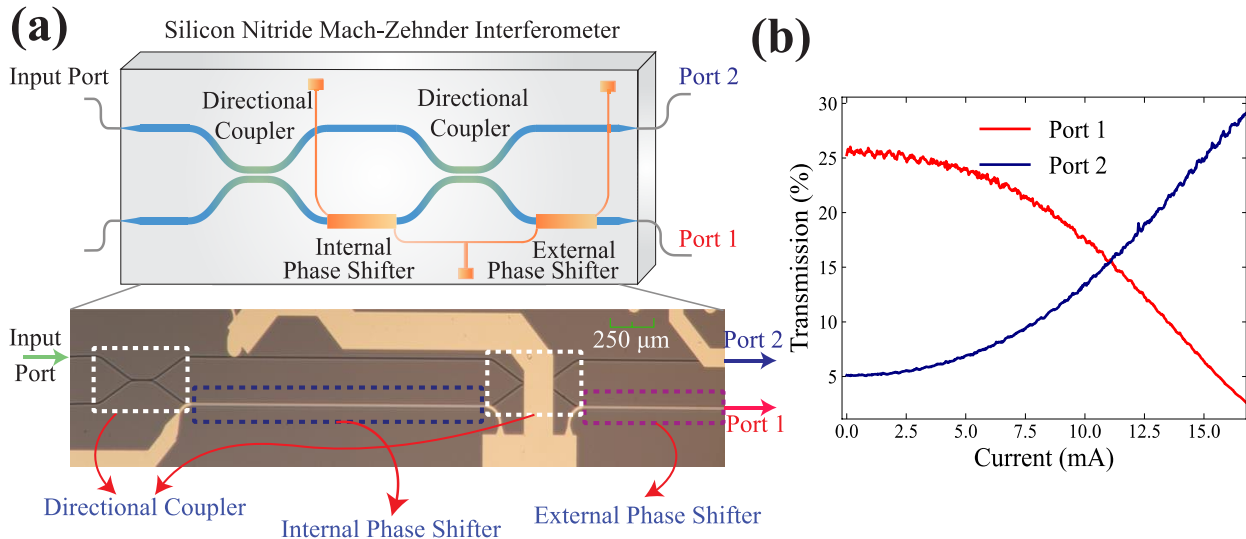
I. Introduction

Trapped ions excel as a platform for quantum networking [1–6]. They exhibit long qubit coherence times [7], high-fidelity single- and two-qubit gates [8,9] as well as the ability to generate single photons entangled with their internal qubit states [3,4,10,11]. Moreover, they can be trapped in compact surface traps [12,13] with integrated waveguides and grating couplers to deliver the light required for cooling and coherent operations [14–16] and close-proximity detectors for state detection [17]. But integrating these discrete memories into a quantum network requires scalable methods to route single photons between different network nodes [1,18].

44
45
46
47
48
49
50
51
52
53
54
55
56
57
58
59
60
61
62
63
64
65
66

Integrated photonic devices offer a compact and scalable solution to realize quantum interconnects that can route photons between nodes of a trapped ion quantum network [19,20]. These devices can act as reconfigurable optical cross-connect switches that control the path of photonic qubits within the network in a programmable way [1,18]. However, the use of integrated photonics to route photons from trapped ions has remained a challenge because their emission typically lies in the ultra-violet and visible wavelength regimes [3,10,11,21,22]. This emission is incompatible with the majority of active photonic integrated circuit platforms, which are mainly designed to work at telecommunication wavelengths [23,24].

In this work, we demonstrate the routing of single photons from a trapped ion using a photonic integrated circuit designed to operate at the telecom C-band. To convert the visible wavelength emission of the ion to the single-mode operating condition of the photonic integrated circuit, we employ a two-stage quantum frequency conversion process [25]. We actively route photons between different output ports of the circuit with a total transmission of $31.0 \pm 0.9\%$ through the device. We also implement 50/50 beam splitting, an essential operation for entanglement distribution [1,3,18,26]. Our photonic integrated circuit is fabricated using a commercial foundry, which is compatible with large scaleup [27,28]. The primary purpose of our device is to distribute entanglement over a quantum network, as described by Monroe and Kim [1] via probabilistic photon emission with heralded detection. Our demonstration opens the possibilities for quantum networks where single photons distribute entanglement between trapped ion nodes in a programmable way over long distances with high yield routers.



67
68
69
70
71
72
73
74
75

FIG. 1 Schematic and transmission properties of the Mach-Zehnder interferometer. (a) A schematic of the silicon nitride Mach-Zehnder interferometer along with an optical microscope image. Highlighted white, blue, and purple boxes are the two directional couplers and the internal and external phase shifters, respectively. (b) The transmission of the Mach-Zehnder interferometer measured at the two output ports as a function of current applied to the internal phase-shifter when laser light is coupled into the input port.

II. Experimental Details and Methods

76

77 Figure 1(a) shows the schematic of the photonic integrated circuit along with an optical
78 microscope image of the device. The device consists of a Mach-Zehnder interferometer composed
79 of two 50/50 directional couplers with a programmable internal phase shifter between them. The
80 external phase shifter at port 1 can be used to adjust the phase difference between output ports,
81 which is important to control two photon interference when distributing entanglement [29]. In our
82 experiments, we set this phase shifter current to 0 mA. The device was fabricated using the
83 standardized Si₃N₄ LioniX TriPleX process with optoelectronic packaging and fiber pigtail. The
84 waveguides in the photonic circuit are double-stripped silicon nitride waveguides, which exhibits
85 low loss. A full description of the waveguide geometry and LioniX TriPleX fabrication process
86 can be found in Ref. [24]. We control the thermo-optic phase shifters using current-driven
87 chromium heaters on the top of the cladding layer above the waveguide. The interferometer has a
88 scalable width of $\sim 250 \mu\text{m}$ and length of $\sim 5.5 \text{ mm}$. The device is housed on a chip of 8 mm by
89 32 mm where it's possible to add ~ 60 more Mach-Zehnder interferometer units.

90

91 **A. Characterization of Mach-Zehnder Interferometer**

92 We first characterize the transmission behavior of the Mach-Zehnder interferometer with a
93 continuous-wave laser operating at a wavelength of 1534 nm. We couple light into the input port
94 and measure the transmission at the output ports 1 and 2 as a function of the current applied to the
95 internal phase shifter (Fig. 1(b)). The current on the internal phase shifter changes the refractive
96 index of the material, creating a phase shift between the top and bottom waveguides. By sweeping
97 the current supplied to the phase-shifter, we can continuously shift the output light from Port 1 to
98 2, achieving a near-maximum transmission out of Port 2 at the device's current limit of 16.6 mA
99 specified by LioniX (Fig. 1(b)). Under this condition, the device draws $\sim 200 \text{ mW}$ power with a
100 bias voltage of 12 V. We achieve a 50/50 splitting ratio with 11.05 mA applied to the internal
101 phase shifter. We determine this current level by finding the point where the red and blue line
102 intersect with each other in Fig. 1(b).

103

104 At the current limit of 16.6 mA, we attain a phase shift ($\Delta \phi$) of 0.82π by fitting the transmission
105 of port 1 to $\cos^2(\Delta \phi)$. Here, the relationship between phase shift and current is given by the
106 relationship $\Delta \phi = \frac{2\pi L}{\lambda} \frac{dn}{dT} \frac{I^2 R_h \tau}{H} + \phi_0$ [30,31]. Here $\Delta \phi$ is the phase shift and I represents the
107 current applied in the internal phase shifter. λ is the operating wavelength and $\frac{dn}{dT}$ corresponds to
108 the change of refractive index(n) with temperature (T). L , R_h , τ and H represent the length,
109 resistance, time constant and heat capacity of the heater respectively. We define ϕ_0 as the constant
110 phase shift between top and bottom waveguides. Higher currents could increase this phase shift
111 but would also exceed the specified damage threshold of the device. This issue can be rectified by
112 increasing the length of the internal phase shifter to achieve a larger phase shift and with the same
113 current.

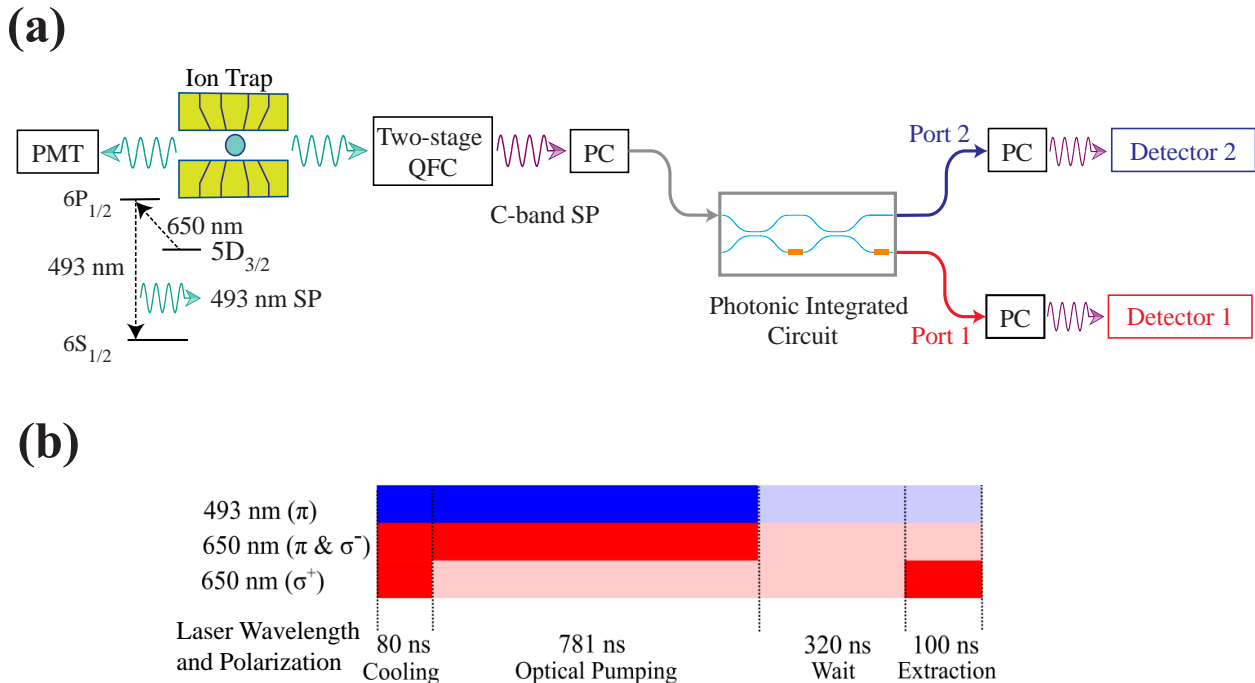
114

115 We define the extinction ratio of each output port as the ratio between their maximum to minimum
116 transmission. Using this definition, the extinction ratios are 10.2 dB and 7.6 dB for Port 1 and Port
117 2 respectively. These imperfect extinction ratios can be attributed to fabrication imperfections in
118 the directional couplers which differ the process parameters like width, etch depth, gap, thin-film
119 thickness, etc. from their intended design value. These imperfections deviate the directional
120 couplers from their ideal 50/50 ratio, hindering the ability to obtain perfect interference and a high

121 extinction ratio. These imperfections can be mitigated by replacing the directional couplers with
 122 active Mach-Zehnder interferometers where the splitting ratio can be actively tuned close to its
 123 ideal value [32]. Using this technique, proposed by David A. Miller [32], Wilkes *et al.*
 124 demonstrated a 60 dB extinction ratio for an on-chip Mach-Zehnder interferometer [33].
 125

126 The imbalance in extinction ratios can result from the imbalanced configuration of the Mach-
 127 Zehnder interferometer. The heater at the bottom waveguide, which controls the phase shift,
 128 creates a loss difference between the top and bottom waveguide in the interferometer resulting in
 129 an imbalance in the extinction ratios. To overcome this imbalance, we could use a balanced
 130 configuration of the Mach-Zehnder interferometer by including heaters in both the top and bottom
 131 waveguides [34].
 132

133 The sum of the transmission from the two output ports is $31.0 \pm 0.9\%$ for all heater currents. The
 134 losses in the device arise from imperfect coupling from the fiber pigtail, waveguide losses, back-
 135 reflection, and optical absorption by the metal contact. This transmission is consistent with the
 136 expected losses in the device including from the input/output facets (<2 dB/facet), the two heating
 137 elements (<0.5 dB each) and the intrinsic material loss (<0.1 dB/cm) specified by LioniX [24].
 138



139 **FIG 2. The experimental layout and timing sequence.** (a) Block diagram illustration of the experimental setup used
 140 to route single photons from a trapped barium ion using a silicon nitride photonic integrated circuit. Here PMT:
 141 photomultiplier tube, QFC: quantum frequency conversion, PC: polarization control, SP: single photons. Also shown
 142 is the basic energy level diagram for $^{138}\text{Ba}^+$ depicting the 493 nm and 650 nm transitions and the emission of a single
 143 photon with a wavelength of 493 nm. Two-stage QFC includes both the quantum frequency conversion stages and
 144 subsequent filtering stage via a 20 GHz bandwidth tunable filter and 46.1 MHz bandwidth etalon. (b) The
 145 experimental timing sequence showing the wavelength and polarization of the various 493-nm and 650-nm beams that
 146 we use to cool, optically pump and extract single 493 nm photons from the trapped barium ion. In this figure, solid
 147 and transparent colors indicate that the lasers are on and off, respectively.
 148
 149

150 B. Experimental Layout and Single Photon Production

151 Figure 2(a) shows a block diagram illustration of the experimental setup used to generate single
152 photons from a trapped ion and couple the emission into the photonic integrated circuit. We first
153 generate 493-nm visible single photons from a trapped barium ion ($^{138}\text{Ba}^+$). The vacuum chamber
154 housing the ion trap has both a front and back reentrant window, allowing for photon collection in
155 two directions. Photons collected from the back window are sent to a photomultiplier tube to
156 measure the temporal photon shape of 493-nm photons throughout the experiment. Photons
157 collected from the front window are sent through a polarizer and converted to 1534 nm using a
158 two-stage quantum frequency conversion system as reported in Ref. [25]. This wavelength is
159 compatible with the single-mode operation of our designed photonic integrated circuit. We then
160 couple converted single photons to the input port of the silicon nitride Mach-Zehnder
161 interferometer. A free-space polarization controller prior to the photonic-integrated circuit's input
162 fiber-coupler aligns the polarization of the photon to the transverse electric-guided mode of the
163 waveguide. We use two superconducting-nanowire single-photon detectors to detect photons at
164 the output ports of the Mach-Zehnder interferometer. Because these detectors are polarization-
165 sensitive, we use additional polarization control stages after the output ports to maximize
166 photodetection efficiency.

167
168 To generate 493 nm single photons from a single barium ion ($^{138}\text{Ba}^+$) we use a scheme as described
169 in prior work [22,25,35]. First we doppler cool the barium ion and then optically pump it into the
170 $|5S_{3/2}, m_s=+3/2\rangle$ state using π and σ^- polarized 650 nm light and π polarized 493 nm light
171 [6,22,25,35]. We then excite the ion using σ^+ polarized 650 nm light to the $|6P_{1/2}, m_j=+1/2\rangle$ state
172 which can spontaneously decay to the $|6S_{1/2}, m_j=\pm 1/2\rangle$ ground state, emitting a 493-nm single
173 photon. This process is repeated at a rate of 780.64 kHz and the relative timings of this sequence
174 is shown in Fig. 2 (b). In this figure, the solid color represents the corresponding laser being on,
175 whereas the transparent color indicates the laser is off. In each cycle of photon production, we wait
176 for 320 ns, directly after optical pumping, with all the lasers being off, to ensure that no stray light
177 is detected during the photon extraction process. The dedicated Doppler cooling time of 80 ns
178 prioritizes the photon production rate over achieving a low ion temperature. That is, the value
179 chosen was the lowest possible time that did not produce a measurable degradation in the emitted
180 photon's coupling into the single mode fiber after the collection lens.

181
182

183 C. Quantum Frequency Conversion

184

185 We use a two-stage quantum frequency conversion scheme to generate telecom C-band photons
186 from the ion. Quantum frequency conversion is the process where the quantum states of two light
187 beams of different frequencies can be interchanged [36]. In quantum frequency conversion, the
188 noise and other parasitic processes are reduced to an extremely low level such that the frequency
189 conversion process preserves the quantum nature of the light [36]. We reported the details of the
190 quantum frequency conversion system in previous work [25]. In the first stage of quantum
191 frequency conversion, we generate 780 nm single photons from 493 nm single photons utilizing a
192 1343 nm pump laser with a conversion efficiency of 20% including filtering at ~ 220 mW pump
193 power [37,38]. Then, in a second stage of conversion, we convert 780 nm single photons to 1534
194 nm single photons using a 1589 nm pump laser. We achieve 25% conversion-efficiency in the
195 second stage of quantum frequency conversion including all filtering at ~ 250 mW pump power.
196 To filter anti-Stokes noise photons produced by spontaneous Raman scattering from the 1589 nm

197 pump laser, we use a 20 GHz bandwidth tunable filter with 80% transmission, and a 46.1 MHz
198 bandwidth etalon with $\sim 60\%$ transmission after the second stage. In both frequency conversion
199 processes, we use a difference frequency generation scheme using periodically poled lithium-
200 niobate waveguides [25,37]. We attain an overall conversion efficiency of 5% in the two-stage
201 frequency conversion scheme.

202
203
204 To stabilize the frequency of the C-band converted photon, we lock the two pump laser frequencies
205 to ensure that the converted photons do not drift outside the bandwidth of the etalon. We first lock
206 a 1762 nm laser to an ultra-low expansion cavity via a Pound–Drever–Hall technique. This locked
207 laser is then used as a reference laser with which we lock the conversion pump lasers. We lock the
208 pump lasers relative to the 1762 nm laser using a Fabry-Perot scanning cavity [39] with a scan
209 frequency of 170 Hz resulting in a drift lock of a few MHz.

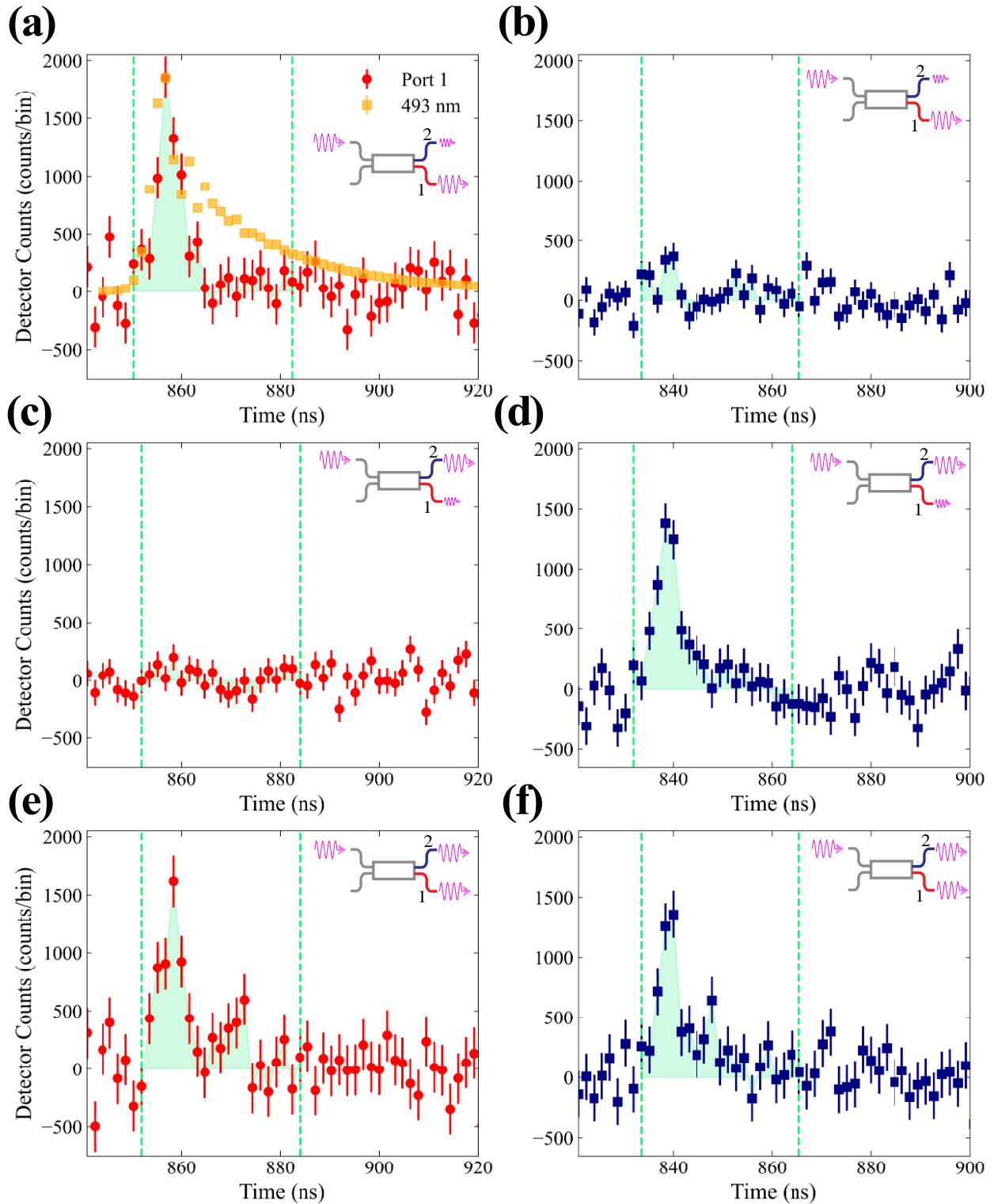
210
211

212 **III. Results**

213
214 Figure 3 shows the time-resolved photon counts at the output ports, relative to a trigger pulse
215 synchronized with the extraction laser pulse. All data are background-subtracted to account for
216 detector dark counts and Raman anti-Stokes noise photons created by the pump laser in the
217 conversion process. The dark counts of detector 1 and 2 are $\sim 110 \pm 20$ counts/sec and $\sim 150 \pm 20$
218 counts/sec, respectively. The pump used in the second-stage of quantum frequency conversion
219 produces noise photons due to undesirable processes such as Raman scattering of the pump. As a
220 result, we detect $\sim 2350 \pm 50$ counts/sec noise photons, measured at the output of the filters to the
221 two-stage conversion and before the photonic integrated circuit using detector 1. This noise is
222 dominated by Raman anti-Stokes noise photons present in the bandwidth of the filtering after two-
223 stage quantum frequency conversion. The proportion of the Raman anti-Stokes noise photons
224 present in each detector channel can be found by considering the respective channel’s transmission
225 from the Mach-Zehnder interferometer.

226
227 Fig. 3(a) shows the time-resolved photon counts measured at Port 1 when the current of the internal
228 phase shifter is set to 0 mA (red circles). The two vertical green dashed lines denote the time
229 window used to measure the photon arrival events. We determine this time window from the
230 temporal shape of the 493 nm photons measured using the photomultiplier tube. We set the window
231 width to be 32 ns, which captures 75% of the total 493-nm photon counts. The red data points
232 show C-band converted photon signal during the window, consistent with the time-resolved 493
233 nm photon counts (gold squares). Fig. 3(b) shows the same trace for C-band converted photons at
234 Port 2 (blue squares). In this case, the histogram shows a large reduction in photon probability,
235 indicating that nearly all single photons are routed to Port 1. Fig. 3(c)-(d) show the same
236 measurements at an internal phase shifter current of 16.6 mA, which corresponds to the reverse
237 condition. Here, the majority of photons exit at Port 2, and we observe only a weak signal at Port
238 1. These measurements demonstrate the routing of single photons from a trapped ion to different
239 output ports of the photonic integrated circuit. Fig. 3(e)-(f) show the time-resolved photon counts
240 at output ports 1 and 2, respectively when we apply a current of 11.05 mA to the internal phase
241 shifter, which corresponds to the 50/50 splitting condition. In this case, we measure the time-
242 resolved photon counts at both ports with similar amplitudes. The run time for data taken with the

243 photonic integrated device's internal shifter set to 0 mA (Fig.3(a) and (b)) 16.6 mA (Fig.3(c) and
244 (d)) and 11.05 mA (Fig.3(e) and (f)) were 10.34 hours, 9.56 hours, and 19.44 hours respectively.
245 Using the peak counts/bin shown in Fig. 3 and the run times, we get a total count rate within the
246 peak bin of 179 counts/hour, 145 counts/hour, and 153 counts/hour for three current conditions,
247 with variations attributed to different alignment settings between days.
248
249

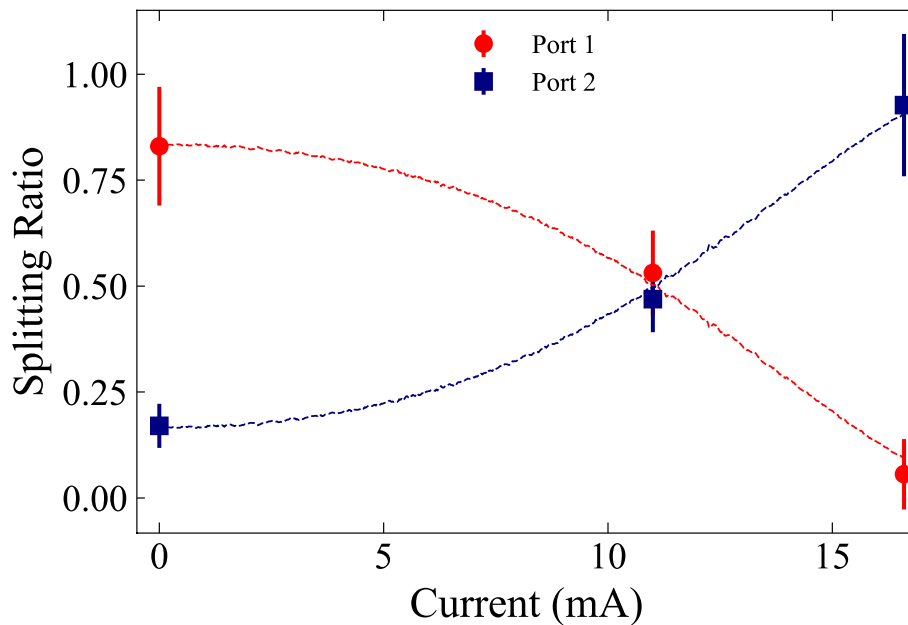


250
 251
 252
 253
 254
 255
 256

FIG. 3 The temporal photon shapes at the output ports of the Mach-Zehnder interferometer at different current levels of the internal phase shifter. (a) and (b) are the time-resolved photon counts at Port 1 (red circles) and Port 2 (blue squares) when the interferometer is set at the maximum transmission of Port 1 (0 mA current on the internal phase shifter). In these plots, the horizontal axis shows the time difference between the arrival of the photon and the trigger pulse. We also plot the scaled version of 493 nm time-resolved photon counts (gold squares) as a reference. (c) and (d) are time-resolved photon counts measured at Port 1 and Port 2 when the internal phase shifter current is set to

257 have nearly maximum transmission at Port 2 (16.6 mA current on the internal phase shifter). (e) and (f) are time-
 258 resolved photon counts measured at Port 1 and Port 2 for a 50/50 splitting condition of the Mach-Zehnder
 259 interferometer (11.05 mA current on the internal phase shifter). The green vertical lines in all plots indicate the
 260 window used to count photon arrival events and correspond to 75% of the total 493 nm time-resolved photon counts.
 261 The green shaded area represents the photon area measured at each output port. We use a 1.6 ns bin size and perform
 262 background subtraction to plot all the time-resolved photon counts. All errors correspond to shot noise-limited
 263 accuracy. The run time for the current condition of 0 mA ((a) and (b)), 16.6 mA ((c) and (d)), and 11.05 mA ((e) and
 264 (f)) were 10.34 hours, 9.56 hours, and 19.44 hours, respectively.

265
 266
 267 Figure 4 shows the splitting ratios of Port 1 and Port 2 measured using the photon areas in Fig. 3
 268 (red circles and blue squares respectively), superimposed over the measured splitting ratio using a
 269 continuous wave laser (red and blue dotted lines). We calculate the splitting ratios by dividing the
 270 counts at each output port by the sum of the counts at both ports. These values are corrected for
 271 mismatch of the photodetection efficiencies between the detectors at Port 1 and Port 2. The ratio
 272 of detection efficiencies of the detector at Port 1 to that at Port 2 is 1.13 ± 0.07 with fiber coupling
 273 and polarization control losses taken into account. The error bars correspond to the shot noise-
 274 limited accuracy based on the photon counts in each measurement. The splitting ratios calculated
 275 from the photon shapes show good agreement with the transmission ratios measured with classical
 276 laser light, within experimental uncertainties. These measurements confirm that we are able to
 277 route single photons from the ion using the photonic integrated circuit in a programmable manner.
 278



279 **FIG. 4** The splitting ratio of the output ports of the Mach-Zehnder interferometer as a function of current applied
 280 to the internal phase shifter. The data points represent the splitting ratio calculated from the background-corrected
 281 time-resolved photon counts in Fig.3. The error bars are calculated from the shot noise of the photon counts. The
 282 dotted red and blue lines show the splitting ratio of Port 1 and 2 measured using classical laser light calculated using
 283 the data in Fig 1(b).

285 IV. Discussion

286

287 In summary, we have demonstrated programmable switching of single photons emitted from a
288 trapped ion between different channels on a photonic integrated chip. Our current proof-of-concept
289 demonstration can be extended in future devices in a straightforward way to include large numbers
290 of Mach-Zehnder interferometers to achieve $N \times N$ cross-connects or other arbitrary unitary matrix
291 transformations [29,40]. In addition to routing, photonic integrated circuits can take on other
292 functionalities such as filtering [41], wavelength division multiplexing [42], and frequency
293 conversion [43]. An ultra-low power high-speed switching of photons could be achieved in devices
294 that use the plasma dispersion effect in silicon modulators [44] at the expense of router
295 transmission efficiency. They can also implement fundamental quantum operations such as
296 photonic Bell-state analysis [1,3,18,26], which is necessary to entangle quantum nodes over long
297 distances. These capabilities could ultimately be used to realize scalable and programmable
298 quantum networks using trapped ion quantum technology.
299

300 Acknowledgments

301
302 **Funding**
303 We would like to acknowledge the support from the National Science Foundation (Grant
304 Nos. OIA2134891, EFMA1741651 and OIA2040695) and the Air Force Office of
305 Scientific Research (Grant Nos. FA95501610421 and FA95501810161).
306

307 **Author contributions:** U. Saha, E. Waks, and J. D. Siverns conceived the idea. U. Saha,
308 M. Prabhu, J. D. Siverns and D. Englund designed the experimental layout and photonic
309 integrated circuits. U. Saha, J. Hannegan and J. D. Siverns performed the experiment and
310 analyzed the data. All authors contributed to write, edit, and review the manuscript.
311

312 We acknowledge the support from LioniX for fabricating the photonic integrated circuit.
313

314 **Competing interests:** All authors declare no conflict of financial interest.
315

316 All part numbers and company references are given for technical purposes, and their
317 mention does not represent an endorsement on the part of the U.S. government. Other
318 equivalent or better options may be available.
319

320 **Data and materials availability:** All the data and codes that support the finding of this
321 study are available from corresponding author upon request.
322
323

324 References

- 325 [1] C. Monroe and J. Kim, *Scaling the Ion Trap Quantum Processor*, *Science* **339**, 1164 (2013).
326 [2] L.-M. Duan and C. Monroe, *Colloquium: Quantum Networks with Trapped Ions*, *Rev. Mod. Phys.*
327 **82**, 1209 (2010).
328 [3] L. J. Stephenson, D. P. Nadlinger, B. C. Nichol, S. An, P. Drmota, T. G. Ballance, K. Thirumalai, J.
329 F. Goodwin, D. M. Lucas, and C. J. Ballance, *High-Rate, High-Fidelity Entanglement of Qubits*
330 *Across an Elementary Quantum Network*, *Phys. Rev. Lett.* **124**, 110501 (2020).
331 [4] M. Bock, P. Eich, S. Kucera, M. Kreis, A. Lenhard, C. Becher, and J. Eschner, *High-Fidelity*

- 332 *Entanglement between a Trapped Ion and a Telecom Photon via Quantum Frequency Conversion*,
333 Nat. Commun. **9**, 1998 (2018).
- 334 [5] V. Krutyanskiy, M. Meraner, J. Schupp, V. Krcmarsky, H. Hainzer, and B. P. Lanyon, *Light-Matter*
335 *Entanglement over 50 Km of Optical Fibre*, Npj Quantum Information **5**, 1 (2019).
- 336 [6] A. N. Craddock, J. Hannegan, D. P. Ornelas-Huerta, J. D. Siversns, A. J. Hachtel, E. A. Goldschmidt,
337 J. V. Porto, Q. Quraishi, and S. L. Rolston, *Quantum Interference between Photons from an Atomic*
338 *Ensemble and a Remote Atomic Ion*, Phys. Rev. Lett. **123**, 213601 (2019).
- 339 [7] P. Wang, C.-Y. Luan, M. Qiao, M. Um, J. Zhang, Y. Wang, X. Yuan, M. Gu, J. Zhang, and K. Kim,
340 *Single Ion Qubit with Estimated Coherence Time Exceeding One Hour*, Nat. Commun. **12**, 233
341 (2021).
- 342 [8] T. P. Harty, D. T. C. Allcock, C. J. Ballance, L. Guidoni, H. A. Janacek, N. M. Linke, D. N. Stacey,
343 and D. M. Lucas, *High-Fidelity Preparation, Gates, Memory, and Readout of a Trapped-Ion*
344 *Quantum Bit*, Phys. Rev. Lett. **113**, 220501 (2014).
- 345 [9] C. J. Ballance, T. P. Harty, N. M. Linke, M. A. Sepiol, and D. M. Lucas, *High-Fidelity Quantum*
346 *Logic Gates Using Trapped-Ion Hyperfine Qubits*, Phys. Rev. Lett. **117**, 060504 (2016).
- 347 [10] B. B. Blinov, D. L. Moehring, L.-M. Duan, and C. Monroe, *Observation of Entanglement between a*
348 *Single Trapped Atom and a Single Photon*, Nature **428**, 153 (2004).
- 349 [11] J. D. Siversns, X. Li, and Q. Quraishi, *Ion--Photon Entanglement and Quantum Frequency*
350 *Conversion with Trapped Ba+ Ions*, Appl. Opt. **56**, B222 (2017).
- 351 [12] B. Lekitsch, S. Weidt, A. G. Fowler, K. Mølmer, S. J. Devitt, C. Wunderlich, and W. K. Hensinger,
352 *Blueprint for a Microwave Trapped Ion Quantum Computer*, Sci Adv **3**, e1601540 (2017).
- 353 [13] J. D. Siversns and Q. Quraishi, *Ion Trap Architectures and New Directions*, Quantum Inf. Process.
354 **16**, 314 (2017).
- 355 [14] K. K. Mehta, C. D. Bruzewicz, R. McConnell, R. J. Ram, J. M. Sage, and J. Chiaverini, *Integrated*
356 *Optical Addressing of an Ion Qubit*, Nat. Nanotechnol. **11**, 1066 (2016).
- 357 [15] R. J. Niffenegger, J. Stuart, C. Sorace-Agaskar, D. Kharas, S. Bramhavar, C. D. Bruzewicz, W. Loh,
358 R.T.Maxson, R. McConnell, D. Reens et al., *Integrated Multi-Wavelength Control of an Ion Qubit*,
359 Nature **586**, 538 (2020).
- 360 [16] K. K. Mehta, C. Zhang, M. Malinowski, T.-L. Nguyen, M. Stadler, and J. P. Home, *Integrated*
361 *Optical Multi-Ion Quantum Logic*, Nature **586**, 533 (2020).
- 362 [17] S. L. Todaro, V. B. Verma, K. C. McCormick, D. T. C. Allcock, R. P. Mirin, D. J. Wineland, S. W.
363 Nam, A. C. Wilson, D. Leibfried, and D. H. Slichter, *State Readout of a Trapped Ion Qubit Using a*
364 *Trap-Integrated Superconducting Photon Detector*, Phys. Rev. Lett. **126**, 010501 (2021).
- 365 [18] C. Monroe, R. Raussendorf, A. Ruthven, K. R. Brown, P. Maunz, L.-M. Duan, and J. Kim, *Large-*
366 *Scale Modular Quantum-Computer Architecture with Atomic Memory and Photonic Interconnects*,
367 Phys. Rev. A **89**, 022317 (2014).
- 368 [19] J. Wang, F. Sciarrino, A. Laing, and M. G. Thompson, *Integrated Photonic Quantum Technologies*,
369 Nat. Photonics **14**, 273 (2019).
- 370 [20] U. Saha and E. Waks, *Design of an Integrated Bell-State Analyzer on a Thin-Film Lithium Niobate*
371 *Platform*, IEEE Photonics J. **14**, 1 (2022).
- 372 [21] P. Kobel, M. Breyer, and M. Köhl, *Deterministic Spin-Photon Entanglement from a Trapped Ion in*
373 *a Fiber Fabry–Perot Cavity*, Npj Quantum Information **7**, 1 (2021).
- 374 [22] C. Crocker, M. Lichtman, K. Sosnova, A. Carter, S. Scarano, and C. Monroe, *High Purity Single*
375 *Photons Entangled with an Atomic Qubit*, Opt. Express **27**, 28143 (2019).
- 376 [23] A. E.-J. Lim, J. Song, Q. Fang, C. Li, X. Tu, N. Duan, K. K. Chen, R. P.-C. Tern, and T.-Y. Liow,
377 *Review of Silicon Photonics Foundry Efforts*, IEEE J. Sel. Top. Quantum Electron. **20**, 405 (2014).
- 378 [24] C. G. H. Roeloffzen, M. Hoekman, E. J. Klein, L. S. Wevers, R. B. Timens, D. Marchenko, D.
379 Geskus, R. Dekker, A. Alippi, R. Grootjans et al., *Low-Loss Si₃N₄ TriPleX Optical Waveguides:*
380 *Technology and Applications Overview*, IEEE J. Sel. Top. Quantum Electron. **24**, 1 (2018).
- 381 [25] J. Hannegan, U. Saha, J. D. Siversns, J. Cassell, E. Waks, and Q. Quraishi, *C-Band Single Photons*
382 *from a Trapped Ion via Two-Stage Frequency Conversion*, Appl. Phys. Lett. **119**, 084001 (2021).

- 383 [26] D. L. Moehring, P. Maunz, S. Olmschenk, K. C. Younge, D. N. Matsukevich, L.-M. Duan, and C.
384 Monroe, *Entanglement of Single-Atom Quantum Bits at a Distance*, *Nature* **449**, 68 (2007).
- 385 [27] W. Bogaerts, Y. Xing, and U. Khan, *Layout-Aware Variability Analysis, Yield Prediction, and*
386 *Optimization in Photonic Integrated Circuits*, *IEEE J. Sel. Top. Quantum Electron.* **25**, 1 (2019).
- 387 [28] P. Muñoz, P.W.L van Dijk, D. Geuzebroek, M. Geiselmann, C. Domínguez, A. Stassen, J. D.
388 Doménech, M. Zervas, A. Leinse, C. G. H. Roeloffzen et al., *Foundry Developments Toward Silicon*
389 *Nitride Photonics From Visible to the Mid-Infrared*, *IEEE J. Sel. Top. Quantum Electron.* **25**, 1
390 (2019).
- 391 [29] N. C. Harris, G. R. Steinbrecher, M. Prabhu, Y. Lahini, J. Mower, D. Bunandar, C. Chen, F. N. C.
392 Wong, T. Baehr-Jones, M. Hochberg et al., *Quantum Transport Simulations in a Programmable*
393 *Nanophotonic Processor*, *Nat. Photonics* **11**, 447 (2017).
- 394 [30] M. Prabhu, *Towards Optimal Capacity-Achieving Transceivers with Photonic Integrated Circuits*,
395 Massachusetts Institute of Technology, 2018.
- 396 [31] N. C. Harris, Y. Ma, J. Mower, T. Baehr-Jones, D. Englund, M. Hochberg, and C. Galland, *Efficient,*
397 *Compact and Low Loss Thermo-Optic Phase Shifter in Silicon*, *Opt. Express* **22**, 10487 (2014).
- 398 [32] D. A. B. Miller, *Perfect Optics with Imperfect Components*, *Optica*, *OPTICA* **2**, 747 (2015).
- 399 [33] Wilkes, Qiang, Wang, Santagati, and Paesani, *60 dB High-Extinction Auto-Configured Mach–*
400 *Zehnder Interferometer*, *Opt. Lett.* (2016).
- 401 [34] Y. Shen, N. C. Harris, S. Skirlo, M. Prabhu, T. Baehr-Jones, M. Hochberg, X. Sun, S. Zhao, H.
402 Larochelle, D. Englund, M. Soljačić, *Deep Learning with Coherent Nanophotonic Circuits*, *Nat.*
403 *Photonics* **11**, 441 (2017).
- 404 [35] J. D. Siversns, X. Li, and Q. Quraishi, *Ion–photon Entanglement and Quantum Frequency*
405 *Conversion with Trapped Ba⁺ Ions*, *Appl. Opt.* **56**, B222 (2017).
- 406 [36] P. Kumar, *Quantum Frequency Conversion*, *Opt. Lett.* **15**, 1476 (1990).
- 407 [37] J. D. Siversns, J. Hannegan, and Q. Quraishi, *Neutral-Atom Wavelength-Compatible 780 Nm Single*
408 *Photons from a Trapped Ion via Quantum Frequency Conversion*, *Phys. Rev. Applied* **11**, 014044
409 (2019).
- 410 [38] J. D. Siversns, J. Hannegan, and Q. Quraishi, *Demonstration of Slow Light in Rubidium Vapor Using*
411 *Single Photons from a Trapped Ion*, *Sci Adv* **5**, eaav4651 (2019).
- 412 [39] J. J. McLoughlin, A. H. Nizamani, J. D. Siversns, R. C. Sterling, M. D. Hughes, B. Lekitsch, B. Stein,
413 S. Weidt, and W. K. Hensinger, *Versatile Ytterbium Ion Trap Experiment for Operation of Scalable*
414 *Ion-Trap Chips with Motional Heating and Transition-Frequency Measurements*, *Phys. Rev. A* **83**,
415 013406 (2011).
- 416 [40] W. R. Clements, P. C. Humphreys, B. J. Metcalf, W. Steven Kolthammer, and I. A. Walmsley,
417 *Optimal Design for Universal Multiport Interferometers*, *Optica*, *OPTICA* **3**, 1460 (2016).
- 418 [41] W. Bogaerts, P. De Heyn, T. Van Vaerenbergh, K. De Vos, S. Kumar Selvaraja, T. Claes, P. Dumon,
419 P. Bienstman, D. Van Thourhout, and R. Baets, *Silicon Microring Resonators*, *Laser Photon. Rev.* **6**,
420 47 (2012).
- 421 [42] C. A. Brackett, *Dense Wavelength Division Multiplexing Networks: Principles and Applications*,
422 *IEEE J. Sel. Areas Commun.* **8**, 948 (1990).
- 423 [43] Y. Hu, M. Yu, D. Zhu, N. Sinclair, A. Shams-Ansari, L. Shao, J. Holzgrafe, E. Puma, M. Zhang, and
424 M. Lončar, *On-Chip Electro-Optic Frequency Shifters and Beam Splitters*, *Nature* **599**, 587 (2021).
- 425 [44] W. M. Green, M. J. Rooks, L. Sekaric, and Y. A. Vlasov, *Ultra-Compact, Low RF Power, 10 Gb/s*
426 *Silicon Mach-Zehnder Modulator*, *Opt. Express* **15**, 17106 (2007).

427

428